Supplementary information for: Tunable corrugated patterns in an active nematic sheet

Anis Senoussi,[†] Shunnichi Kashida,[†] Raphael Voituriez,[†,‡] Jean-Christophe Galas,[*,†] Ananyo Maitra,[*,†] and André Estevez-Torres[*,†]

†*Sorbonne Université and CNRS, Laboratoire Jean Perrin, F-75005, Paris, France*

‡*Sorbonne Université and CNRS, Laboratoire de Physique Théorique de la Matière Condensée, F-75005, Paris, France*

E-mail: jean-christophe.galas@upmc.fr; nyomaitra07@gmail.com; andre.estevez-torres@upmc.fr

Contents

Other supplementary materials for this manuscript include the following

Movies S1 to S4

1 Methods

Chemicals and reagents

All chemicals and reagents were purchased from Sigma-Aldrich, New England Biolabs, Roche, and ThermoScientific.

Kinesins expression

From the plasmid coding for the K430 truncated kinesin-1 (amino acid residues 1-430) from Rattus norvegicus designed by Furuta et al. (*1*), we have built a homodimer version containing a SNAP-tag on each arm. Furuta's plasmid, pET-32ark430(C7S)-FlagC-rk430(C7S)-SnapC-His, which expresses both Kinesin-Snap-His and Kinesin-Flag was digested at two EcoRI sites to split into two fragments of Kinesin-Flag sequence and Kinesin-Snap-His with backbone sequence coding ampicillin resistance gene. The digested linear sequences were purified by QIAquick PCR Purification Kit (Qiagen) and recircularized by T4 DNA ligase using Rapid DNA Ligation Kit (Thermo Scientific). The recircularized plasmids were transformed into DH5α competent cells and selected on 100 μg/mL ampicillin including agar plate. The plasmids in colonies on agar plate were amplified in LB ampicillin medium and purified with Monarch Plasmid Miniprep Kit protocol (New England Biolabs). The sequence was verified by restriction enzyme digestion.

Homodimer K430 was expressed in competent cells, Rosetta2 (DE3) (Novagen). The cells were cultured in LB supplemented with 100 μg/mL Ampicilin and 34 μg/mL Chloramphenicol at 37 °C until OD660 = 0.6. The protein expression was induced by 0.1 mM IPTG for 5 hours at 22 °C. The cells were collected and resuspended in the Lysis Buffer: Buffer A (20 mM Na-Pi buffer pH 7.5, 1 mM $MgSO_4$, 250 mM NaCl, 0.015 mM ATP, 10 mM β-mercaptoethanol, 0.1 % Tween-20) supplemented with 10 mM imidazole and 1X protease inhibitor cocktail (Sigma-Aldrich). The cell suspension was then sonicated (VCX-130, Sonics Materials) and centrifuged. The supernatant was collected and filtrated before mixing with

Ni-IMAC resin (Biorad). The resin was washed first with the Buffer A and 10 mM imidazole, and then with the same buffer but with 50 mM of imidazole. The resin was eluted with the Buffer A supplemented with 250 mM imidazole. The eluate was filtrated and filled in 14 kDa MWCO cellulose tube (Sigma-Aldrich) and then dialyzed with Buffer A three times (2 times 1 hour and overnight) at 4 °C. The dialyzed protein was further purified with a Superdex 200 Increase column (GE Healthcare). The kinesin corresponding peak fraction was collected, flash-frozen and kept at −80 °C.

For K401 purification, pT7-7_DmKinesin 1-401 BCCP-CHis6 (pWC2) plasmid designed by Gelles J. J (*2*) was expressed in competent cells Rosetta2 (DE3) (Novagen). The cells were cultured in LB supplemented with 100 μM biotin, 100 μg/mL ampicillin and 34 μg/mL chloramphenicol at 37 °C until OD660 = 0.7. The protein expression was induced by 1 mM IPTG for 2 hours at 22 °C and then the biotinylation was induced by 0.2 mM rifampicin for 20 hours at 22 °C. The cells were collected and resuspended in the Buffer B (50 mM PIPES pH 7.2, 4 mM $MgCl_2$, 50 μM ATP, 10 mM β-mercaptoethanol) supplemented with 20 mM imidazole and 1X protease inhibitor cocktail (Sigma-Aldrich). The cell suspension was then sonicated (VCX-130, Sonics Materials) and centrifuged. The supernatant was collected and filtrated before mixing with Ni-IMAC resin (Biorad). The resin was washed with the Buffer B and 20 mM imidazole. The resin was eluted with the Buffer B and 500 mM imidazole. The eluate was filled in Float-A-Lyzer G2 (5 mL; 50K MWCO, Spectora/Por), dialyzed with Dialysis Buffer (250 mM PIPES pH 6.7, 20 mM $MgCl_2$, 0.25 mM ATP, 50 mM β-mercaptoethanol) three times (1 hour, 2.5 hours and overnight) at 4 °C. The dialyzed protein supplemented with 36 % sucrose and 2 mM dithiothreitol (DTT) was flash-frozen and kept at −80 °C.

Microtubule polymerization

Tubulin and TRITC-labeled tubulin were purchased from Cytoskeleton, dissolved at 10 mg/mL in 1X PEM buffer (80 mM PIPES pH 6.8, 1 mM EGTA, 1 mM $MgSO_4$) supplemented

with 1 mM GTP, flash-frozen and stored at −80 °C. The polymerization mix consists of 1X PEM, 1 mM GTP, 10 % (w/v) glycerol and microtubules at 5 mg/mL (including 2.5 % fluorescent tubulin). First the mix was centrifugated at 4 °C for 15 min at 16000 g to remove small aggregates of tubulin. The corresponding supernatant was transferred into a new tube and incubated at 37 °C for 15 min. 20 μM of paclitaxel (in the following taxol) was added to the mix and let at 37 °C for five more minutes. After polymerization, newly formed microtubules were centrifugated at room temperature for 10 min at 12000 g to remove free tubulin monomers. The microtubules were redissolved into 1X PEM, 1 mM GTP, 10 % glycerol, 20 μM taxol and kept in the dark at room temperature for few days.

For control experiments, GMPCPP (Jena Bioscience) microtubules were polymerized in the presence of 0.5 mg/mL GMPCPP from tubulin at 37 °C for 30 min and left at room temperature for 5 hours. They were used within the same day.

2 Hydrodynamic theory of an undulating active film

In this section, we discuss an active fluid model (*3–6*) to understand the buckling of the effectively two-dimensional sheet formed by the microtubules and obtain a theoretical estimate for the scaling of the wavelength of the undulatory pattern with motor concentration. The thickness of the nematic film, lying parallel to the the xy plane, in the z direction is denoted by ℓ_z and the channel thickness in the z direction by H. The width of the channel in the y direction is W and the length along x is L. The film is formed by injecting an isotropic microtubule fluid into the channel of dimensions $L \times W \times H$. The interaction mediated by depletion agents in the fluid then leads to the phase separation of the microtubule filaments and the fluid with a local concentration of filaments that exceeds the threshold for isotropic-nematic (I-N) transition. Due to the geometry of the channel, the nematic order develops along the long x axis, leading to the formation of a film which contracts along the y and z direction and extends along the x direction. This leads to a nematic film which is the thinnest along the z direction. The orientation of the nematic is described by the director field $\hat{\mathbf{n}} = cos\,\phi\,\hat{x} + sin\,\phi\,\hat{z} = \hat{\mathbf{n}}_0 + \delta\mathbf{n}$, with the unbuckled state having the director $\hat{\mathbf{n}}_0 = \hat{x}$.

This film buckles along the z direction due to the action of motors. We will now describe the physics of this buckling. We assume that the density of microtubules within the layer is fixed. We further assume that the nematic film buckles in the z direction as whole. The departure of the mid-plane of the film from a fiducial flat surface which we take to be the mid-xy plane of the channel is described by the height field $h(x, y, t)$ of the membrane point whose projection on that fiducial plane has the coordinates (x, y). Such a buckling is possible due to tilting of the microtubule filaments in the xz plane $\delta\mathbf{n} \approx \partial_x h\hat{z}$ to linear order.

In equilibrium, tilting of filaments is penalised by the Frank elasticity (*7*), considered here within a simplifying one Frank-constant approximation, which yields a bending modulus of the film:

$$F_{\rm Frank} = \frac{\bar{K}}{2}\int d^3\mathbf{r}(\nabla\hat{\mathbf{n}})^2 \approx \frac{K}{2}\int d^2\mathbf{x}(\partial_x^2 h)^2. \quad (1)$$

where $K = \bar{K}\ell_z$ and $\mathbf{x}$ describes the $x-y$ plane. The membrane is confined in a channel of height H, which means that its mean-squared height fluctuations $\langle h^2\rangle \sim H^2$. Following (*8–10*), we implement this constraint in an approximate manner by introducing a harmonic potential $(\gamma/2)h^2$ in the effective free energy of the membrane i.e.,

$$F_h = \frac{1}{2}\int d^2\mathbf{x}\left[K(\partial_x^2 h)^2 + \gamma h^2\right]. \quad (2)$$

In equilibrium at a temperature T, equating the mean-squared fluctuation with H^2 yields $\gamma = (K_B T/8H^2)^2/K$. The membrane does not have a passive surface tension since we assume that it is free to adjust its area to maintain the preferred areal density of microtubules due to the depletion forces constant (*11*). However, in the experiments in which the channel is confined in the x direction as well, the microtubule sheet may have a pattern even in the absence of motors due to Euler buckling. Since this is only manifested for channels confined along the x axis and vanishes in other cases, we ignore this passive effect from here on and instead focus on the motor-driven periodic corrugation of the active membrane.

We model the dynamics of an active membrane with the passive restoring forces arising from the derivative of a free-energy given by eq. (2). Since the membrane is suspended in a fluid, it moves due to the motion of the fluid. Since h represent the height of a membrane point above a fiducial surface, $\dot{h} \sim v_z|_m$ where $v_z|_m$ is the z component of the fluid velocity at the membrane position. For the linear theory that we are interested in here, $v_z|_m$ can be approximated by $v_z(0)$ the z component of the velocity at the position of the fiducial plane. However, if fluid can pass (permeate) through the membrane, fluid flow need not correspond to the motion of the membrane. This relative velocity of the fluid and a passive membrane is $\propto \mu\delta F_h/\delta h$, where μ is the permeation coefficient. In addition, active membranes may move relative to the background fluid due to an active speed $\sim -\mu\bar{\zeta}(c)\hat{\mathbf{n}}_0\cdot\nabla\delta\mathbf{n} \approx -\mu\bar{\zeta}(c)\partial_x^2 h\hat{z}$

(*12*). For extensile filaments, the active coefficient, whose magnitude depends on the motor concentration, $\bar{\zeta}(c) > 0$. Thus, the hydrodynamic equation for h is

$$\dot{h} - v_z(0) = -\mu \frac{\delta F_h}{\delta h} - \mu \bar{\zeta}(c) \partial_x^2 h \tag{3}$$

The Stokes equation for the velocity field containing the membrane composed of active units is

$$\eta \nabla^2 \mathbf{v} = \nabla \Pi + \zeta(c) \nabla \cdot (\mathbf{nn}) \delta(z) + \frac{\delta F_h}{\delta h} \hat{z} \delta(z) \approx \nabla \Pi + \left(\zeta(c) \partial_x^2 h + \frac{\delta F_h}{\delta h} \right) \hat{z} \delta(z) + \boldsymbol{\xi}_v \tag{4}$$

where Π is the pressure that enforces the incompressibility constraint $\nabla \cdot \mathbf{v} = 0$, ζ is the coefficient of the standard active stress $\zeta(c) > 0$ for extensile systems. Note that, in principle, $\zeta(c)$ and $\bar{\zeta}(c)$ can be different from each other, though their dependence on motor concentration is expected to be the same. To obtain the second approximate equality, we have ignored all fluctuations of the nematic director in the xy plane (we will discuss the consequence of this approximation later).

The fluid is in a channel of thickness H. We now use the Fourier transformed version of eq. (4) to calculate $v_z(0)$ by summing over all Fourier modes for which $|q_z| > 2\pi/H$, which takes the constraint due to the channel into account in an approximate manner. Eliminating the pressure by projecting the Fourier transformed velocity transverse to the wavevector direction, we obtain

$$v_z(0) = \frac{-1}{2\pi\eta} \left[\int_{\frac{2\pi}{H}}^{\infty} dq_z \frac{q_x^2}{(q_x^2 + q_z^2)^2} G_z(q_x) + \int_{-\infty}^{-\frac{2\pi}{H}} dq_z \frac{q_x^2}{(q_x^2 + q_z^2)^2} G_z(q_x) \right] \tag{5}$$

where $G_z(q_x)$ is the Fourier transform of $\zeta(c)\partial_x^2 h + \delta F_h / \delta h$. This yields

$$v_z(0) = -\frac{1}{4\eta |q_x|} \left[1 - \frac{4H|q_x|}{4\pi^2 + H^2 q_x^2} - \frac{2}{\pi} \tan^{-1} \left(\frac{2\pi}{H|q_x|} \right) \right] G(q_x) \tag{6}$$

The effective mobility goes to $-1/4\eta|q_x|$ in the limit $H \to \infty$ (*13*) and $\sim q_x^2 H^3$ for $q_x H \ll 1$

(*14*, *15*). The force

$$G(q_x) = (Kq_x^4 - \zeta(c)q_x^2 + \gamma)h_{\mathbf{q}}. \tag{7}$$

Putting this back in the equation for height fluctuations, and Fourier transforming in space and time, we obtain

$$\omega = -\frac{i}{4\eta|q_x|}\left[1 - \frac{4H|q_x|}{4\pi^2 + H^2q_x^2} - \frac{2}{\pi}\tan^{-1}\left(\frac{2\pi}{H|q_x|}\right)\right](Kq_x^4 - \zeta(c)q_x^2 + \gamma) - i\mu(Kq_x^4 - \bar{\zeta}(c)q_x^2 + \gamma) \tag{8}$$

Since both the hydrodynamic mobility and the permeation coefficient μ are always positive, we clearly see that extensile activity leads to a positive growth rate for a band of wavenumbers. If permeation dominates over hydrodynamics, a band of wavevectors between

$$q_{x_\pm}^2 = \frac{\bar{\zeta}_c \pm \sqrt{\bar{\zeta}^2 - 4K\gamma}}{2} \tag{9}$$

is unstable. Note that, unlike usual active planar instabilities, the instability here is not long wavelength i.e., the membrane is stable for $q_x \to 0$ due to the confinement. The fastest growing mode is

$$q_x^* = \sqrt{\frac{\bar{\zeta}(c)}{2K}}. \tag{10}$$

We identify this with the wavevector of the pattern we observe. Further, it is known (*16*) that active forces scale as c^2. This implies that the wavelength of the buckled pattern should scale linearly with c, i.e., $\lambda = 2\pi/q^* \propto c$. This linear scaling is observed in our experiments.

If hydrodynamics dominates over permeation (such that permeation can be ignored), the unstable band of wavevectors is given by (9), but with $\bar{\zeta}(c)$ replaced by $\zeta(c)$. Furthermore, in the limits $Hq_x \to \infty$ and $Hq_x \to 0$, the fastest growing mode is

$$q_x^* = \sqrt{\frac{\zeta(c)}{2K}}. \tag{11}$$

While the observed selected wavelength in our system is in neither regime, $Hq_x = 2\pi H/\lambda \sim$

$\mathcal{O}(1)$, we do not believe that this will significantly change the scaling with ζ. Further, since $\zeta(c)$ and $\bar{\zeta}(c)$ should scale the same way with c, the scaling of the wavelength of the pattern with c remains the same, $\lambda \propto c$ for both permeation dominated and hydrodynamics dominated cases. However, the hydrodynamics dominated and the permeation dominated cases can be distinguished by looking at the dependence of the characteristic frequency on activity. For the permeation dominated case,

$$i\omega^* \sim \mu(K q_x^{*4} - \bar{\zeta}(c) q_x^{*2} + \gamma). \tag{12}$$

This implies that $i\omega^* \sim \bar{\zeta}^2 \sim c^4$. For the hydrodynamics dominated case, and for $q_x H \gg 1$, $i\omega^* \sim \zeta^{3/2} \sim c^3$ while for $q_x H \ll 1$, $\omega^* \sim \zeta^3 \sim c^6$.

We have primarily discussed the fluctuation of the thin film along the z direction. The film also contracts along the y direction. A similar theory could be constructed for the undulations of the film in the y direction as well. Since the film is thicker in this direction, thus having a larger bending modulus, $K_w \sim \bar{K} w$, where w is the width of the film, these undulations have a longer wavelength since $q_w^* \sim 1/\sqrt{K_w}$ and $K_w > K \implies q_w^* < q^*$. However, when the anisotropy of the channel is reduced such that $W \sim H$ and therefore, $w \sim \ell_z$, buckling in both y and z direction should be observed simultaneously and should have roughly equal wavelengths. Ultimately, at high activities the coupling of undulations in y and z directions leads to the destruction of the periodically modulated state. Finally, We have not considered the fluctuation of the nematic order of the microtubules in the plane of the membrane. Taking into account such fluctuations is complicated (see (*17*, *18*)) and, in any case, would not change the linear physics of the membrane modulation discussed here.

3 Figures S1 to S15

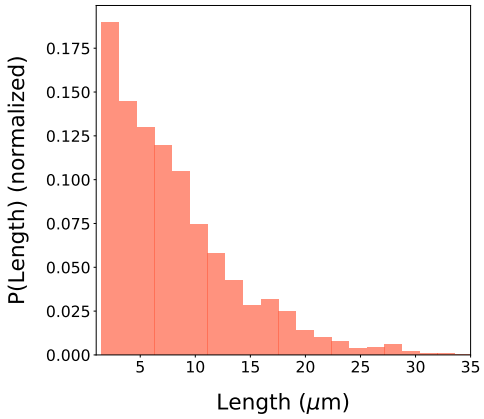

Figure S1: Normalized probability distribution of taxol-stabilized microtubules in our experiments. Microtubules have an average length of 8.1 μm with a standard deviation of 5.8 μm.

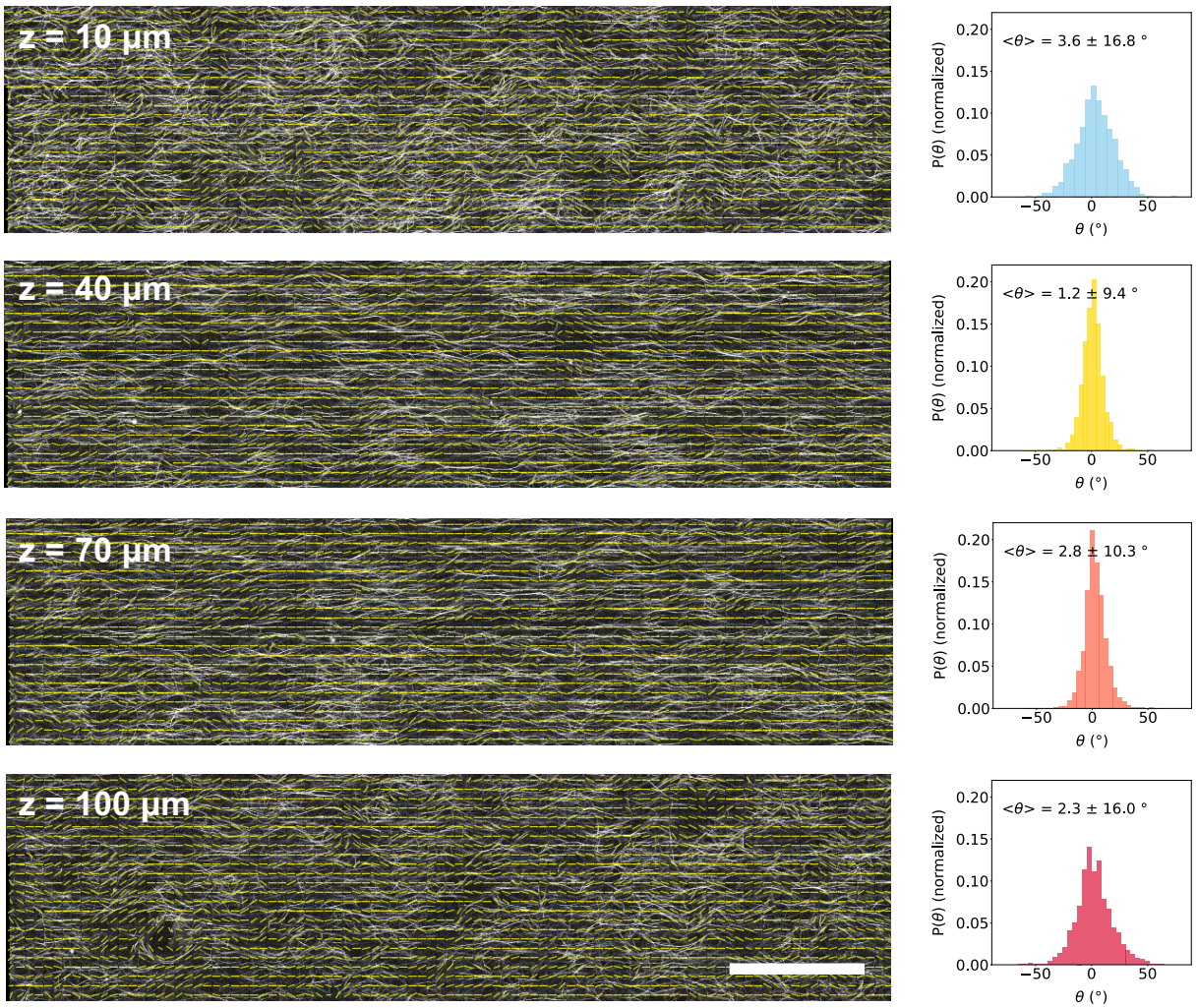

Figure S2: Initial orientation of microtubules in the xy plane for different heights in a flow cell. Orientational fields and distributions were obtained using OrientationJ plugin(*19*) for ImageJ. θ is the angle between the filaments and the x axis in the xy plane. Scale bar 250 μm.

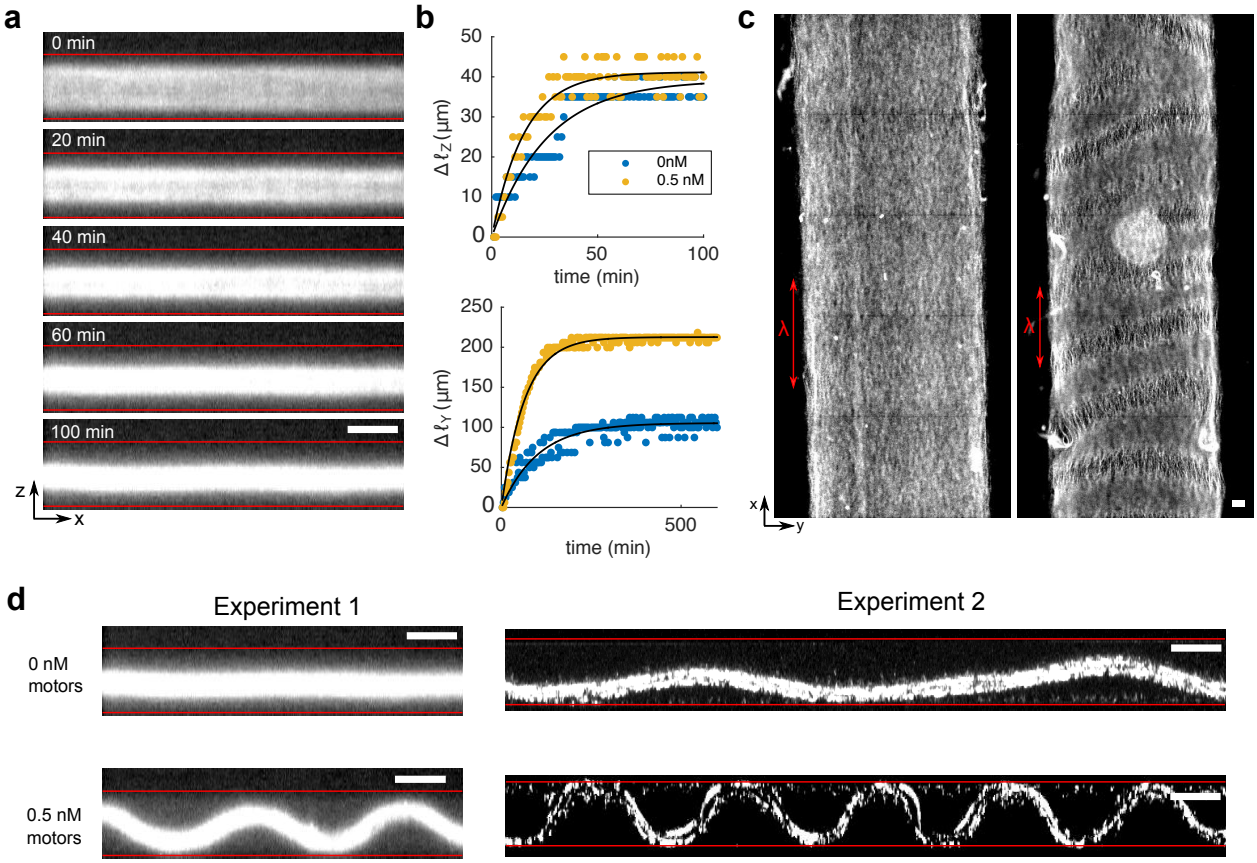

Figure S3: Passive formation of the gel sheet and comparison of the buckling in the passive and active case, including reproducibility. a. Time-lapse confocal fluorescence images of the passive gel in the xz plane. b. Comparison of contractions along z (top) and y (bottom) between gels with and without motors. $\Delta\ell_z^{max}$ was undistinguishable while $\Delta\ell_y^{max}$ and the rates ω_z and ω_y were two-fold smaller in the absence of motors (Table S1). c. Epifluorescence images in the absence (left) and in the presence (right) of motors show focused and defocused bands resulting from buckling with λ indicating the wavelength. The pattern in the absence of motors is faint. d. Buckling reproducibility for experiments performed in a 3 weeks interval with different batches of microtubules. The extent of buckling in the absence of motors is variable (top) while it is fairly reproducible in its presence (bottom). We attribute this variability to a lack of control on the rugosity of the boundaries. Indeed, passive gels might be pinned to surface irregularities that would increase buckling. Scale bars are 100 μm.

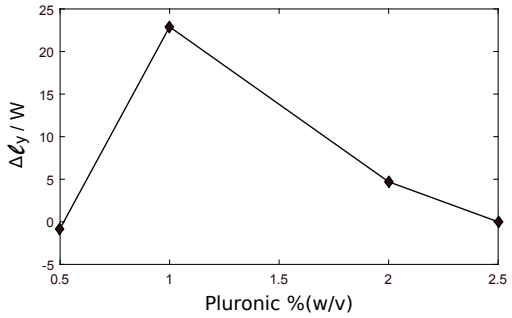

Figure S4: Gel contraction along the y-axis as a function of pluronic concentration. Contraction depends non-monotonically on the concentration of the depletion agent, with a maximum at 1 %(w/v) pluronic concentration.

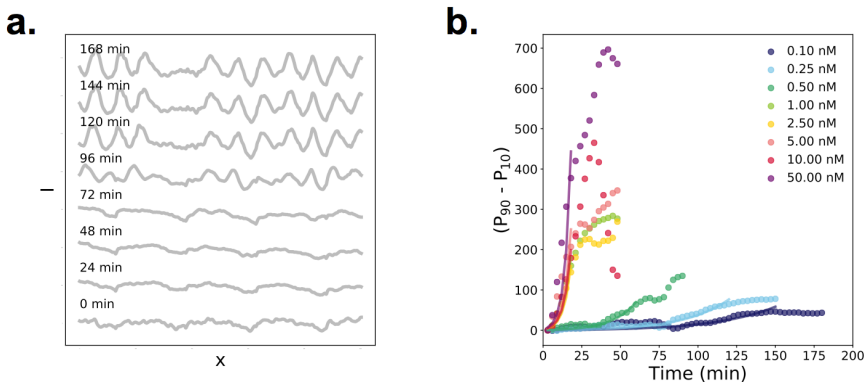

Figure S5: Determination of the growth rate of the pattern ω. **a**. Epifluorescence images were used for the determination of ω. For each time we averaged among y-axis 10 to 50 intensity profiles. **b**. We quantified the temporal formation of the pattern as a change in the distribution of intensities among these profiles: we computed P_{90} and P_{10}, respectively the 90th and the 10th percentile of intensitites, for each time and for each concentration of kinesin. ω was then determined from the fit $(P_{90} - P_{10})(t) = e^{\omega(t+5)} - 1$.

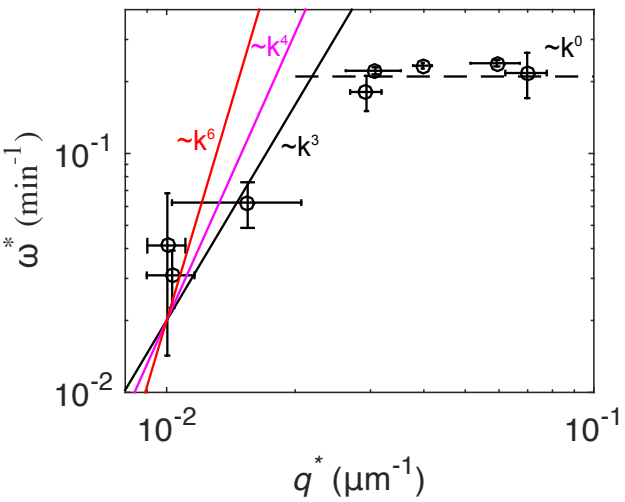

Figure S6: Log-log plot of the wavenumber q^* *vs.* the growth rate ω^*. The lines correspond to different scaling laws.

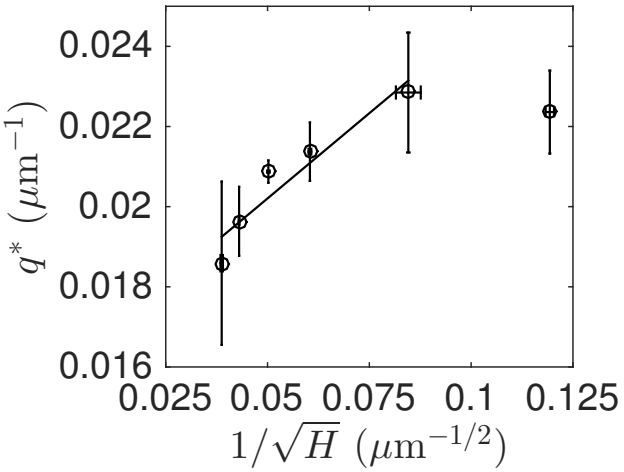

Figure S7: Wavenumber q^* vs. height of the channel H. Error bars correspond to the standard deviation of a triplicate experiment. The line is a linear fit to the first five points. This Figure replots in a different way the data in Figure **??**.

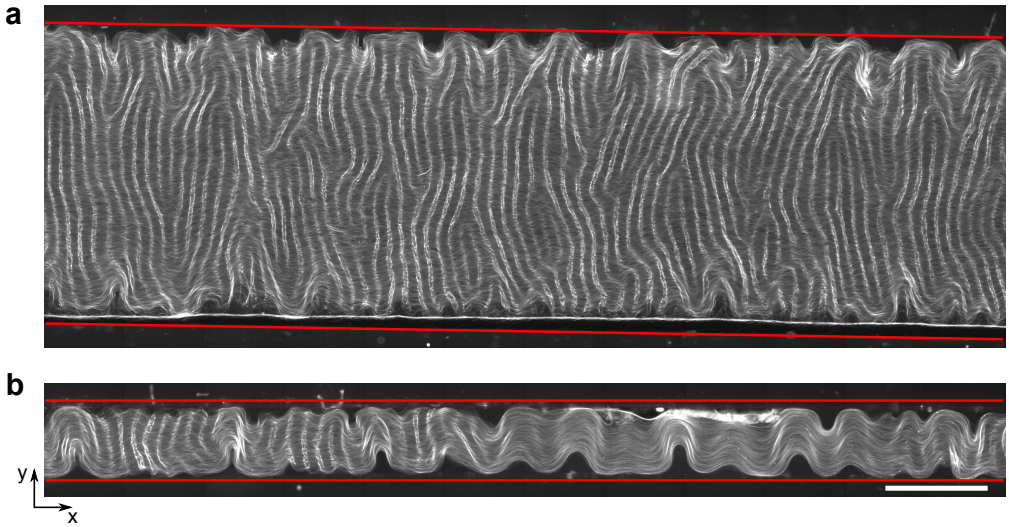

Figure S8: The pattern depends on channel width. Fluorescence image of the gel after 39 min with 0.5 nM motors for channels of different width: 2.9 (**a**) and 0.6 mm (**b**), and the same height (0.13 mm). Red lines indicate channel walls. Scale bar is 1 mm.

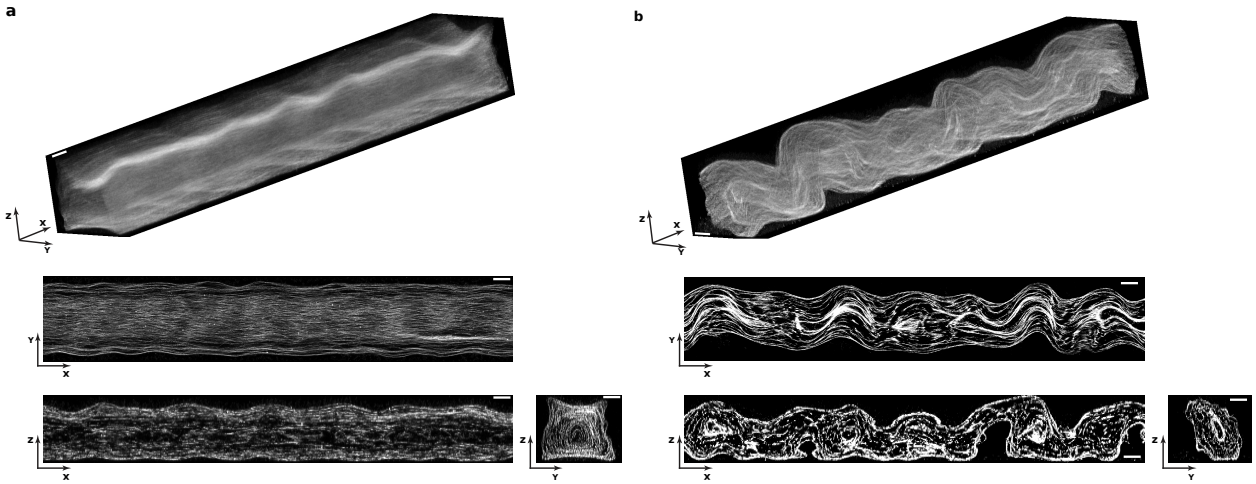

Figure S9: Confocal images of the fluid at final time in a capillary of square section 0.5×0.5 mm^2. **a** 0 nM and **a** 0.5 nM motors. Scale bars are 100 μm. Motor concentration 1 nM.

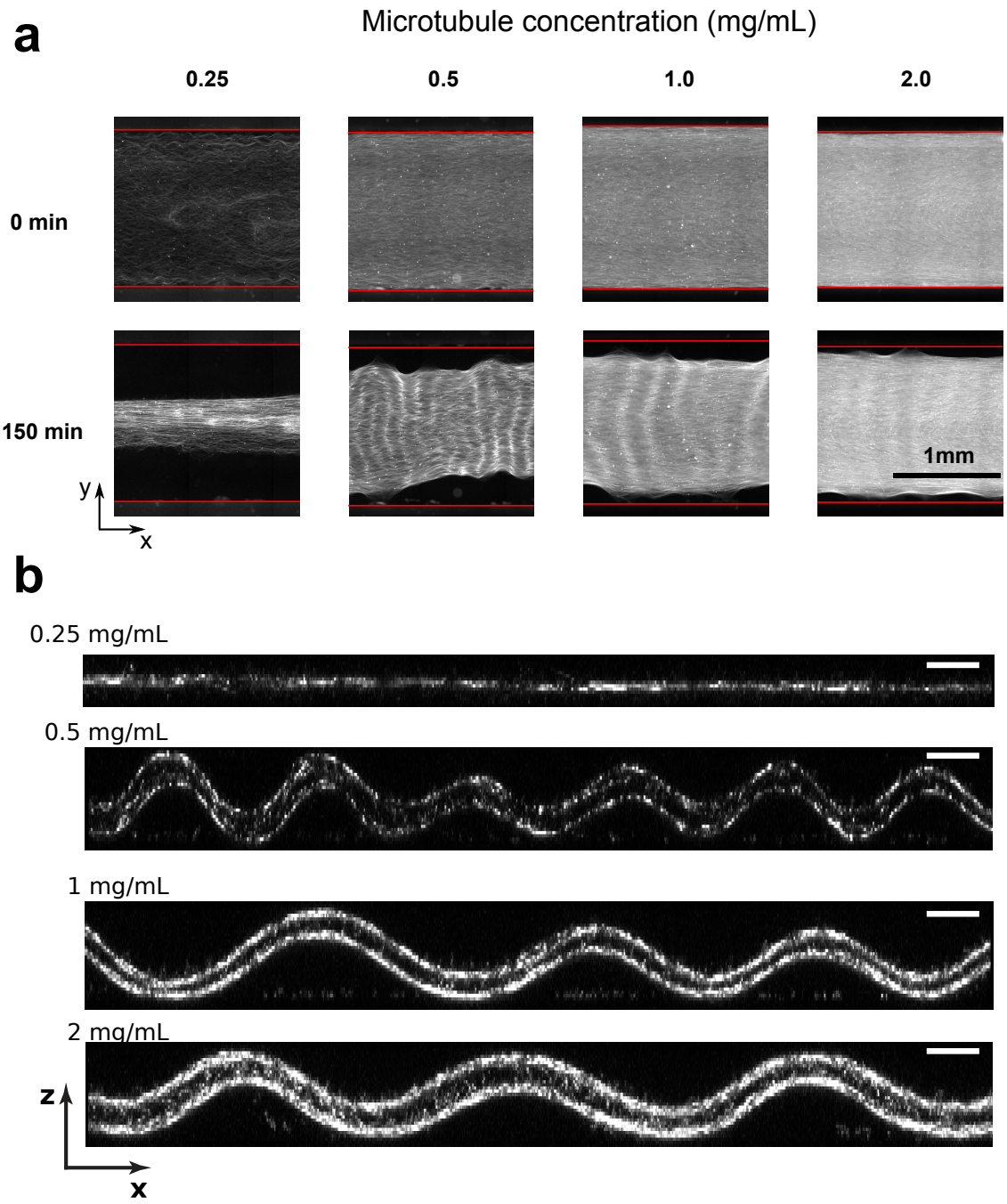

Figure S10: Effect of the microtubule concentration on the observed patterns in epifluorescence (**a**) and confocal microscopy (**b**). At 0.25 mg/mL no corrugation are observed but a strong contraction of the whole system. At higher concentrations, the wavelength of the corrugations increases with increasing microtubule concentration. The brightness of the images at high microtubule concentration has been decreased in order to see the patterns at all concentrations. 1 nM motors. Scale bars in **b** are 100 μm.

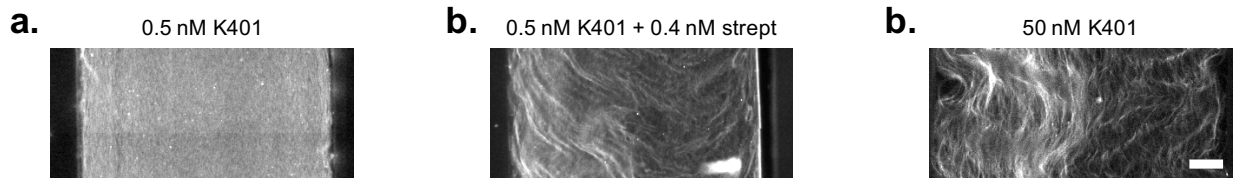

Figure S11: Corrugated patterns are observed with the standard motor K401. a. No patterns were obtained using K401 - that bears a biotin that binds to tetrameric streptavidin forming K401 clusters - at 0.5 nM without streptavidin. b. The addtion of 0.4 nM of streptavidin led to patterns. c. K401 formed periodic patterns at 5 nM in the absence of streptavidin, suggesting that 1 % of K401 make non-specific clusters at these concentrations. Scale bar 250 μm.

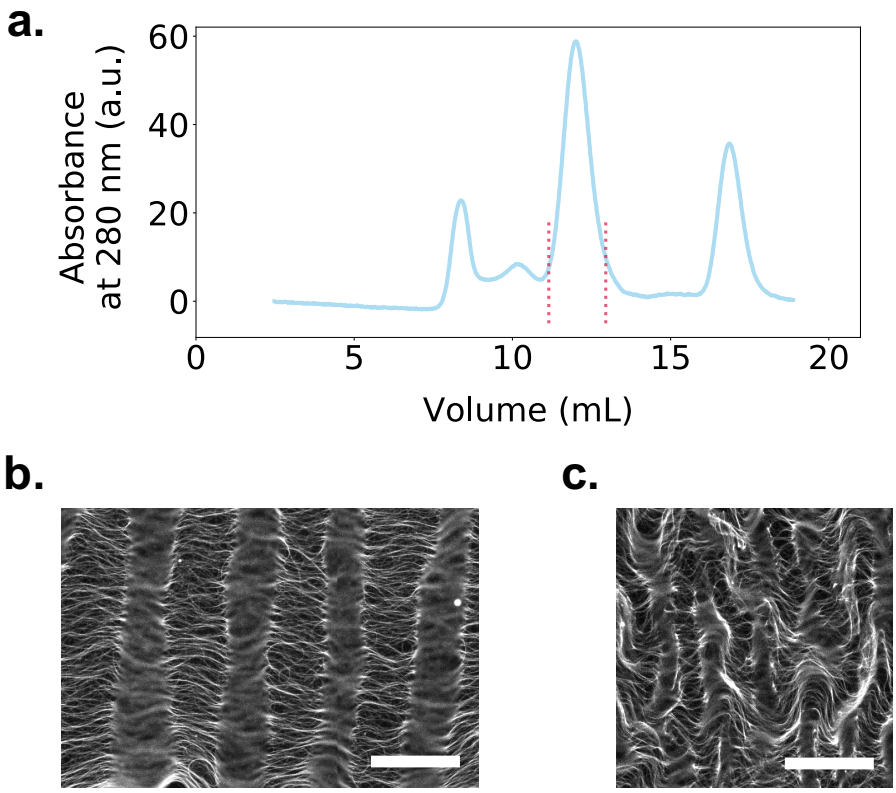

Figure S12: a. Gel filtration profile of dialyzed kinesin. K430 dimers come out at 12 mL (between red dashed lines). Peak at 17 mL corresponds to the SNAP-tag which was produced alone. b. Periodic pattern obtained with 0.22 nM of proteins which were not gel purified (fractions between 7.5 mL and 13 mL). c. Periodic pattern obtained with 14 nM of protein aggregates (peak 8.5 mL). Scale bars 250 μm.

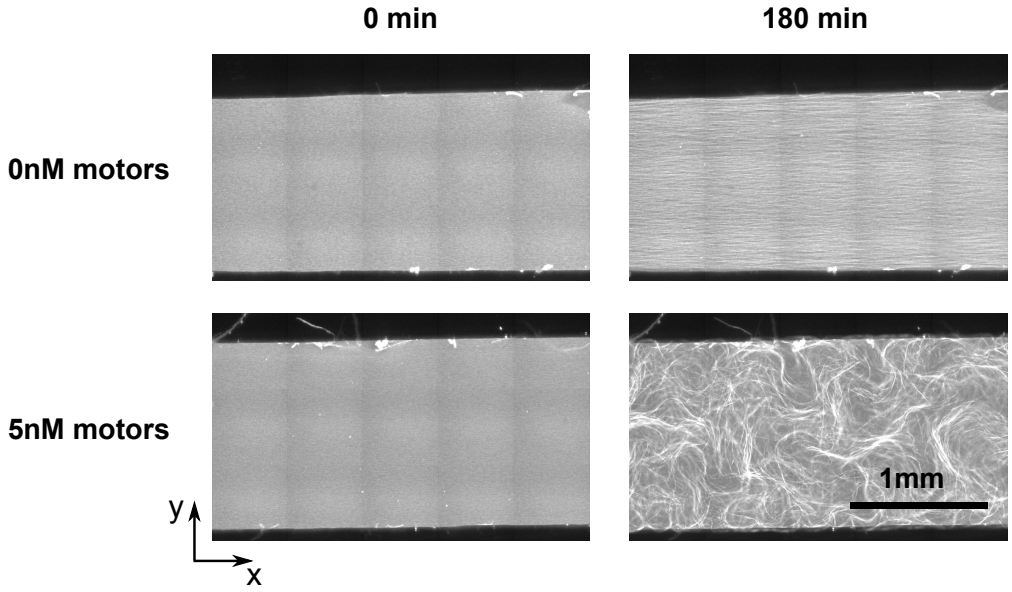

Figure S13: Epifluorescence images of an experiment performed with 1.5 μm-long GMPCPP-stabilized microtubules. No contraction of the gel is observed along y, neither in the presence nor in the absence of motors. Active turbulence is observed at 5 nM motors.

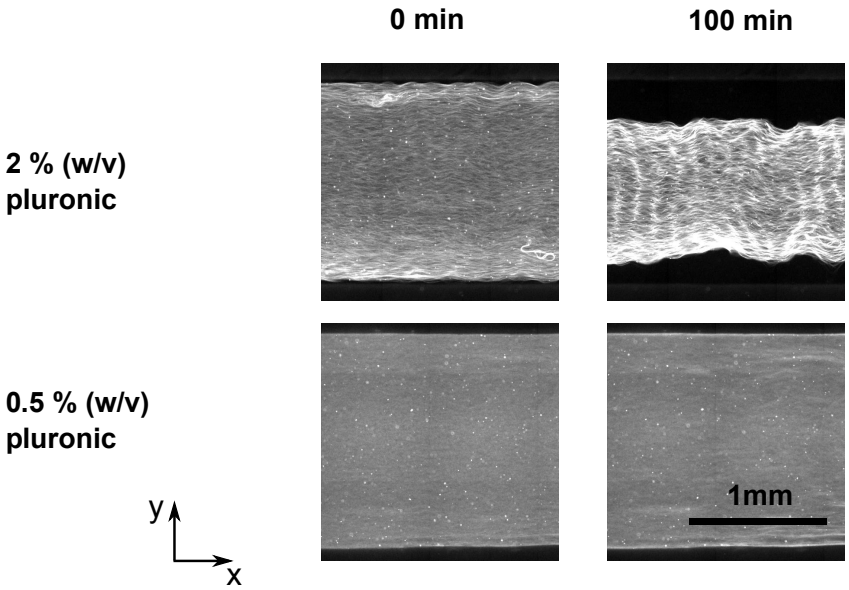

Figure S14: Reducing the attractive force between microtubules by lowering concentration of the depletion agent (pluronic) from standard 2% to 0.5% precludes both buckling and contraction.

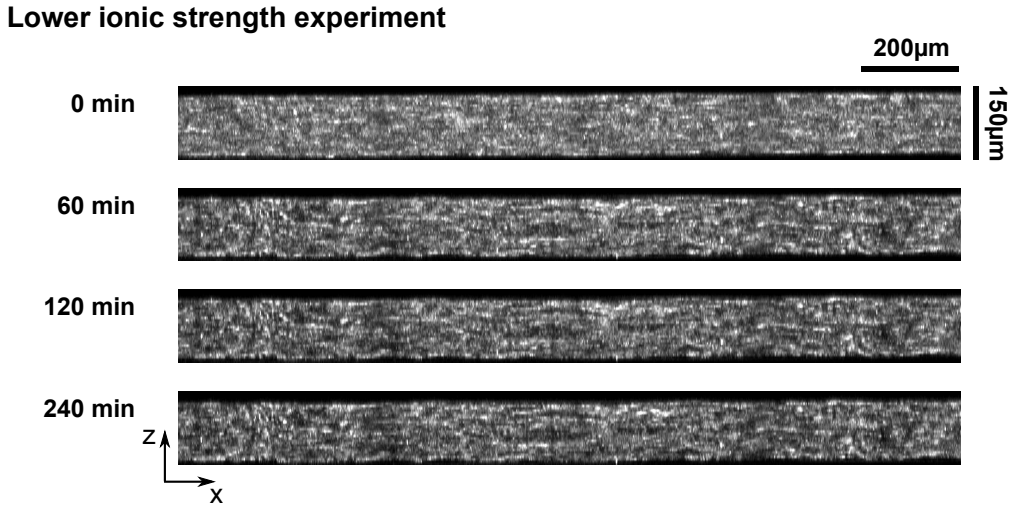

Figure S15: Reducing the attractive force between negatively charged, 8 μm-long, microtubules by lowering the ionic strength of the buffer impede the formation of the thin sheet and the buckling in the xz plane. 0.2X PEM buffer, 2 mM K-acetate, 2 mM KCl, 1 mM $MgCl_2$ were used to prepare the active mix, with 0.5 nM motors, a 1/5 dilution of these components compared to standard conditions.

4 Tables S1 to S2

Table S1: Maximal amplitudes and rates of buckling and contraction for an active (0.5 nM motors) and a passive (0 nM motors) gel.

	Quantity	0.5 nM motors	0 nM motors
Buckling	$\langle\phi^2\rangle^{max}$ (rad^2)	10^{-1}	10^{-3}
	ϕ^{max} (^{o})	32.2 ± 0.5	5 ± 2
	h^{max} (μm)	22 ± 3	1 ± 1
Contraction	$\Delta\ell_z^{max}$ (μm)	40	38
	$\Delta\ell_y^{max}$ (μm)	210	105
	ω_z (10^{-2} min^{-1})	6.4	3.8
	ω_y (10^{-2} min^{-1})	1.5	1.0

Table S 2: Wavelength of the patterns λ , and final thickness of the gel sheet, ℓ_z, as a function of the height of the channel H. We were unable to measure ℓ_z at the largest H. Motor concentration 1 nM.

H (μm)	ℓ_z (μm)	λ (μm)
70.2 ± 1.2	12.2 ± 0.1	281 ± 13
139.8 ± 10.1	50.0 ± 14.6	275 ± 18
274.1 ± 3.1	144.1 ± 22.4	294 ± 10
396.8 ± 4.6	264.0 ± 36.9	301 ± 4
540.5 ± 2.5	413.2 ± 7.9	320 ± 14
666.4 ± 10.30	N.A.	338 ± 37

5 Legends of Movies S1 to S4

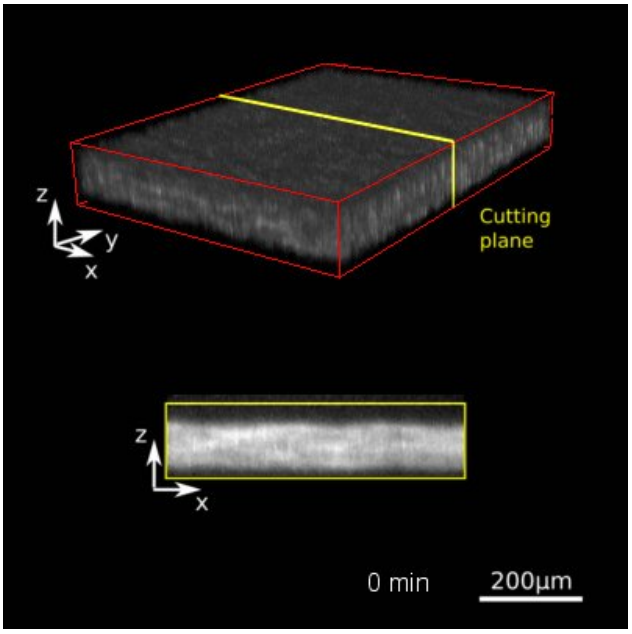

Movie S1: Confocal images and xz sectioning of a 3D extensile, nematic gel made of microtubules and kinesin motors forming a corrugated sheet. Motor concentration is 0.5 nM.

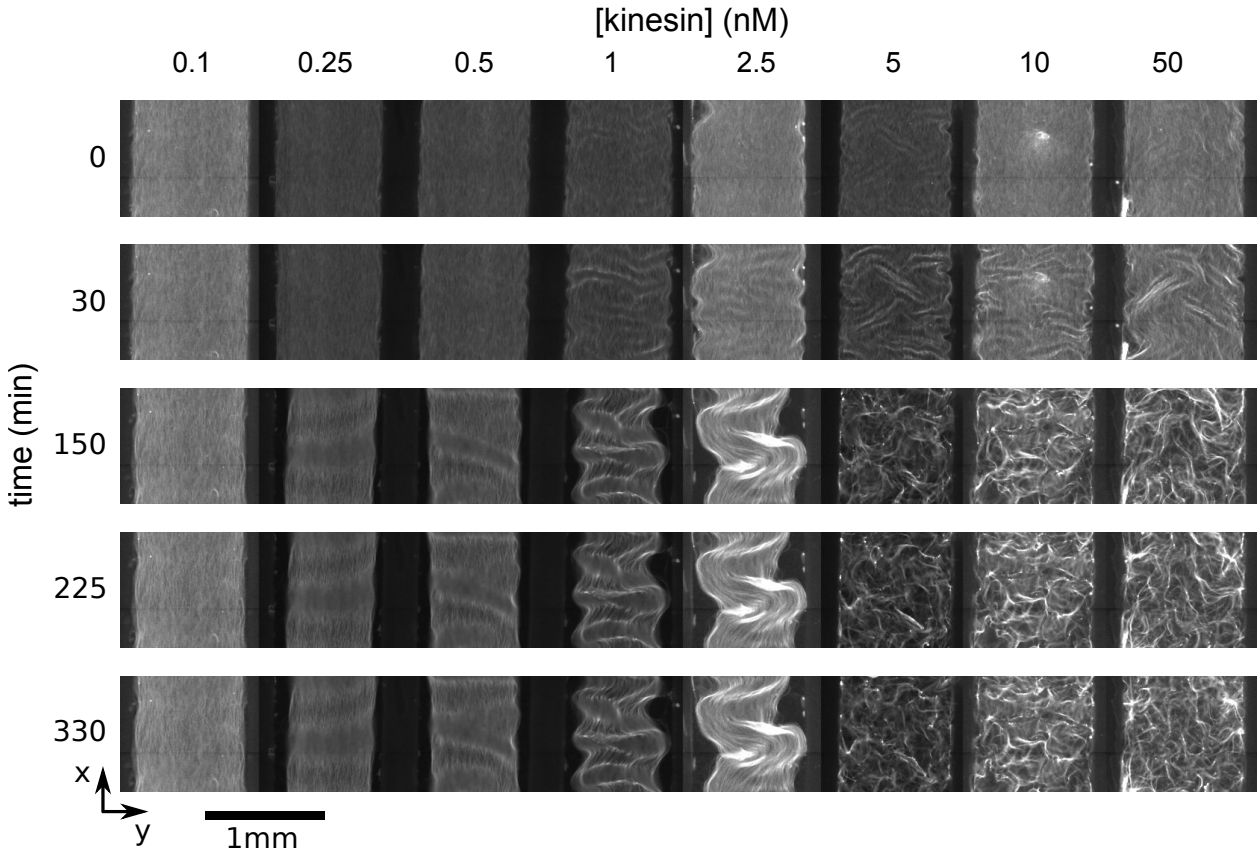

Movie S2: Dynamics, shape and stability of the patterns depending on the motor concentration. The movie shows different channels with different motor concentrations recorded in epifluorescence.

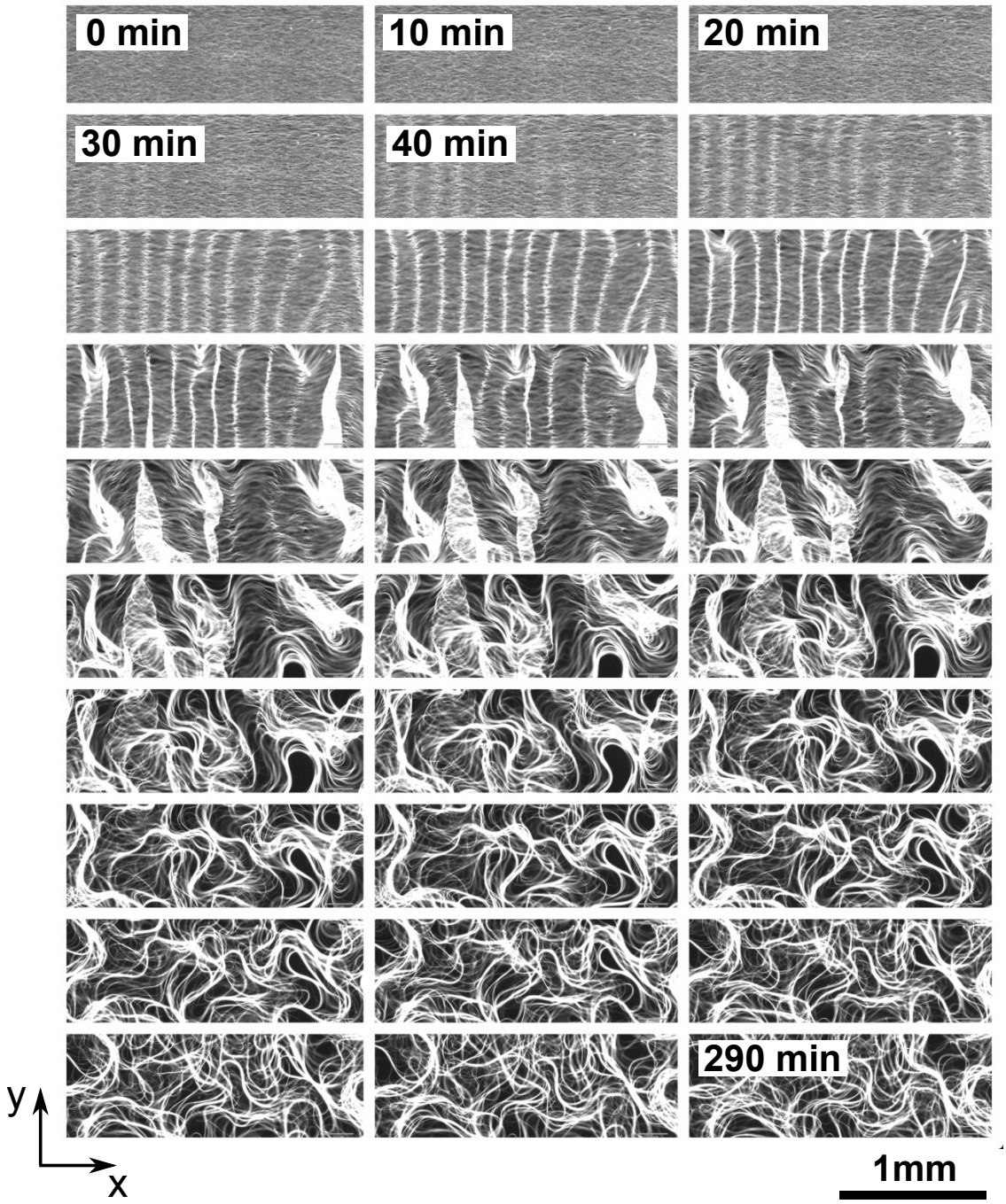

Movie S3: A 3D extensile, nematic gel made of microtubules and kinesin motors forms a corrugated sheet that breaks into active turbulence at high motor concentration. Buckling in the xz plane is observed at early times (stripes at 60 min) then the pattern breaks into an active turbulent state. Epifluorescence time-lapse images in the xy direction. The movie is 10 hours long. This experiment corresponds to a 0.75 nM motor concentration of K430 before size exclusion chromatography and thus its activity is stronger than the rest of the experiments, where purified K430 was used.

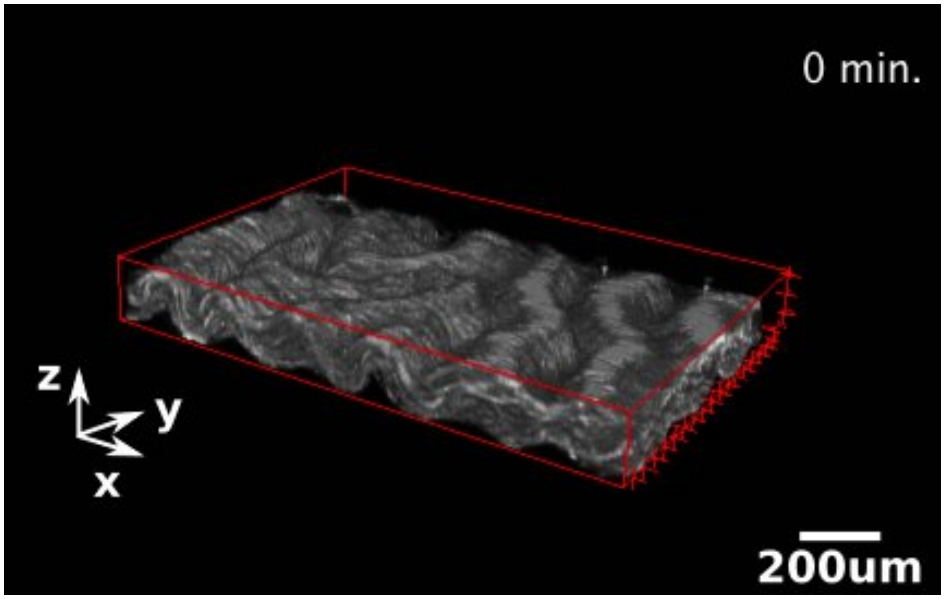

Movie S4: Confocal images of a 3D extensile, nematic gel made of microtubules and kinesin motors forming a corrugated sheet that breaks into active turbulence. Motor concentration is 5 nM. The formation of the corrugated sheet from the initial nematic state is not visible here as it occurs at the very beginning, during the sample preparation.

SI References

1. Furuta, K., Furuta, A., Toyoshima, Y. Y., Amino, M., Oiwa, K., and Kojima, H. (2013) Measuring collective transport by defined numbers of processive and nonprocessive kinesin motors. *Proceedings of the National Academy of Sciences 110*, 501–506.

2. Subramanian, R., and Gelles, J. (2007) Two distinct modes of processive kinesin movement in mixtures of ATP and AMP-PNP. *The Journal of general physiology 130*, 445–455.

3. Marchetti, M. C., Joanny, J. F., Ramaswamy, S., Liverpool, T. B., Prost, J., Rao, M., and Simha, R. A. (2013) Hydrodynamics of soft active matter. *Reviews of Modern Physics 85*, 1143–1189.

4. Ramaswamy, S. (2010) The Mechanics and Statistics of Active Matter. *Annual Review of Condensed Matter Physics 1*, 323–345.

5. Prost, J., Julicher, F., and Joanny, J. F. (2015) Active gel physics. *Nat Phys 11*, 111–117.

6. Jülicher, F., Kruse, K., Prost, J., and Joanny, J.-F. (2007) Active behavior of the Cytoskeleton. *Physics Reports 449*, 3 – 28.

7. de Gennes, P. G., and Prost, J. *The physics of liquid crystals (second edition)*; Oxford university press, 1993.

8. Farago, O. (2008) Membrane fluctuations near a plane rigid surface. *Physical Review E 78*, 051919.

9. Farago, O., and Pincus, P. (2004) Statistical mechanics of bilayer membrane with a fixed projected area. *The Journal of chemical physics 120*, 2934–2950.

10. Fournier, J.-B., and Barbetta, C. (2008) Direct calculation from the stress tensor of the lateral surface tension of fluctuating fluid membranes. *Physical review letters 100*, 078103.

11. Safran, S. *Statistical thermodynamics of surfaces, interfaces, and membranes*; Westview Press, 2013.

12. Maitra, A., Srivastava, P., Rao, M., and Ramaswamy, S. (2014) Activating Membranes. *Phys. Rev. Lett. 112*, 258101.

13. Brochard, F., and Lennon, J. (1975) Frequency spectrum of the flicker phenomenon in erythrocytes. *Journal de Physique 36*, 1035–1047.

14. Gov, N., Zilman, A., and Safran, S. (2004) Hydrodynamics of confined membranes. *Physical Review E 70*, 011104.

15. Seifert, U. (1994) Dynamics of a bound membrane. *Physical Review E 49*, 3124.

16. Martínez-Prat, B., Ignés-Mullol, J., Casademunt, J., and Sagués, F. (2019) Selection mechanism at the onset of active turbulence. *Nature Physics*

17. Nelson, D., and Peliti, L. (1987) Fluctuations in membranes with crystalline and hexatic order. *Journal de physique 48*, 1085–1092.

18. Nelson, P., and Powers, T. (1993) Renormalization of chiral couplings in titled bilayer membranes. *Journal de Physique II 3*, 1535–1569.

19. Rezakhaniha, R., Agianniotis, A., Schrauwen, J. T. C., Griffa, A., Sage, D., Bouten, C. v., Van de Vosse, F., Unser, M., and Stergiopulos, N. (2012) Experimental investigation of collagen waviness and orientation in the arterial adventitia using confocal laser scanning microscopy. *Biomechanics and modeling in mechanobiology 11*, 461–473.